16.5 Elongation rate theorem

The elongation rate describes the change of the depth of the shower maximum per decade in energy [525, 526] and is defined[2] as

$$D_{10} = \frac{\mathrm{d}\langle X_{\max}\rangle}{\mathrm{d}\log_{10} E}. \tag{16.21}$$

It is closely related to possible changes of the cosmic ray composition and also depends on the overall characteristics of hadronic interactions at high energy.

From Eq. 15.29 and the fact that the radiation length in air is 37 g/cm^2, it follows that the elongation rate of electromagnetic showers is $D_{10}^{\mathrm{em}} = \ln(10) \times X_0 \approx 85\,\mathrm{g/cm^2}$ in the energy range in which the LPM effect can be neglected. Assuming that hadronic interactions satisfy Feynman scaling with energy-independent cross sections, the relative energy splitting in the hadronic skeleton of the shower is independent of the primary energy (i.e. it scales with energy). As a consequence, and since the electromagnetic component is dominated by the earliest (i.e. most energetic) generations of hadronic interactions, the elongation rate of the hadronic shower is also D_{10}^{em} in the presence of Feynman scaling.

Validity of Scaling to 10^{20} eV and High-Energy Cosmic-Ray Composition

J. Linsley and A. A. Watson[a]
Department of Physics and Astronomy, University of New Mexico, Albuquerque, New Mexico 87131
(Received 31 July 1980)

It is shown that evidence on cosmic-ray showers of energy 3×10^{16} to 10^{20} eV indicates that scaling in the fragmentation region is valid up to the highest energies if (and only if) hadron-air inelastic cross sections continue to rise in the manner observed at lower energies. It is also shown, with use of additional air-shower evidence, that $\langle \ln A \rangle$, the logarithmic mean primary mass number, changes from (4 ± 2) at 1.6×10^{15} eV to $(0^{+0.6}_{-0})$ at and above 3×10^{16} eV.

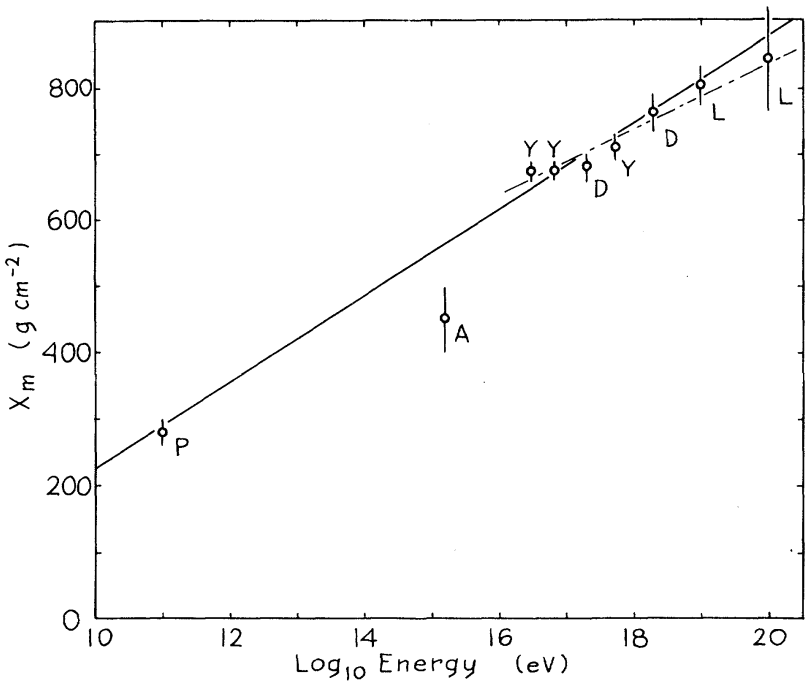

FIG. 1. X_m(g cm^{-2}) as a function of energy. The points above 10^{16} eV are identified in Table I. Point *P*, see text and Ref. 14. Point *A*, see text and Ref. 16. Derivation of the solid and dotted lines is described in the text.

We discuss the data on X_m in terms of D_e, the so-called "elongation rate," equal by definition to $dX_m/d\ln E$. X_m is averaged over fluctuations in shower development, and in case of mixed primary composition over the equal-energy mass spectrum. For numerical results we use "ER

The approximation 15.28 is plotted in Figure 15.2 to illustrate how showers evolve over a wide range of primary energy. Shower maximum occurs for $s = 1$. Therefore from Eq. 15.20 with $n = 0$,

$$X_{\max}^{(\mathrm{em})} = X_0 T_{\max} = X_0 \ln\left(\frac{E_0}{E_c}\right) \tag{15.29}$$

and

$$N_{\max}^{(\mathrm{em})} = \frac{0.31}{\sqrt{\ln(E_0/E_c)}} \frac{E_0}{E_c} \sim 10^6 \left(\frac{E_0(\mathrm{GeV})}{10^6}\right). \tag{15.30}$$

Analogous relations for charged particles in hadron-induced showers will be discussed in the following chapter.

Figure 15.2 shows how Eq. 15.28 for electromagnetic cascades evolves over a wide range of primary photon energy. Similar relations among shower age, depth of maximum and size at maximum can be applied in the analysis of showers initiated by primary cosmic rays.

To obtain a more quantitative estimate we consider the depth of maximum of a proton shower which we approximate by that of the EM subshowers produced by the secondaries of the first interaction, see Eq. 16.3,

$$\langle X^{\rm had}_{\rm max}(E)\rangle = \langle X^{\rm em}_{\rm max}(E/\langle n\rangle)\rangle + \lambda_{\rm int}\ , \tag{16.22}$$

where $\langle n\rangle$ is related to the multiplicity of secondaries in the high-energy hadronic interactions in the cascade. From Eq. 16.22 follows

$$\frac{{\rm d}\langle X^{\rm had}_{\rm max}(E)\rangle}{{\rm d}\log E} = \ln(10) X_0 \left[1 - \frac{{\rm d}\ln\langle n\rangle}{{\rm d}\ln E}\right] + \frac{{\rm d}\lambda_{\rm int}}{{\rm d}\log E}, \tag{16.23}$$

which corresponds to the form of the elongation rate theorem given in Ref. [526], namely

$$D^{\rm had}_{10} \leqslant \ln(10) X_0 (1 - B_n - B_\lambda), \tag{16.24}$$

with

$$B_n = \frac{{\rm d}\ln\langle n\rangle}{{\rm d}\ln E}, \qquad B_\lambda = -\frac{\lambda_{\rm int}}{X_0}\frac{{\rm d}\ln\lambda_{\rm int}}{{\rm d}\ln E}. \tag{16.25}$$

For example, for a multiplicity dependence of $\langle n\rangle \propto E^\delta$ one gets $B_n = \delta$ in the approximation that all secondaries have the same energy.

A Heitler Model – X_{max}

$$X^p_{max} = \lambda_i^{p-air} \ln 2 + X_0 \ln\left(\frac{\kappa E_0}{3 N_{ch} E_c^e}\right)$$

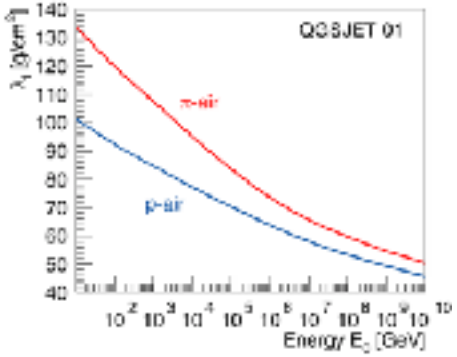

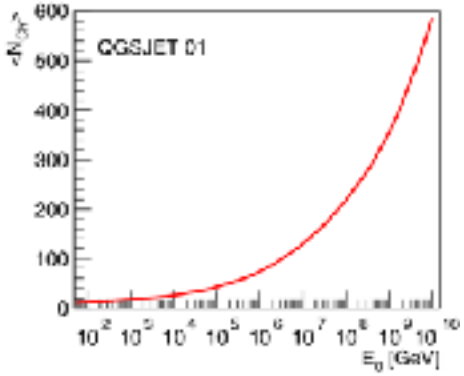

proton air interaction length $\lambda_i^{p-air} = \xi + \zeta \lg \frac{E_0}{\mathrm{PeV}}$ ζ=-4.88 g/cm²

multiplicity of charged particles produced in π-N interactions $N_{ch} = N_0 \left(\frac{E_0}{\mathrm{PeV}}\right)^{\eta}$ η=0.13

$$X^p_{max} = \xi \ln 2 - X_0 \left(\frac{3 N_0 E_c^e}{\kappa \cdot \mathrm{PeV}}\right) + \Lambda^p \lg\left(\frac{E_0}{\mathrm{PeV}}\right)$$

elongation rate

e/m shower $\Lambda^{\gamma} = X_0 \ln 10 \approx 84.4 \mathrm{g/cm}^2$

proton shower

$\Lambda^p = X_0 \ln 10 - \eta X_0 \ln 10 + \zeta \ln 2 \approx 70 \mathrm{g/cm}^2$

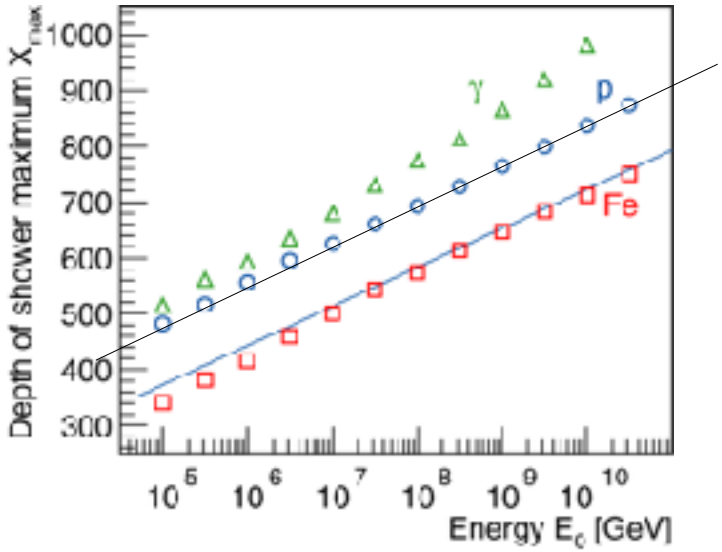

X_{max} for heavy nuclei

$$X^A_{max} = X^p_{max} - X_0 \ln A$$

➡ **estimator for mass *A* of primary particle**

J. Matthews, Astrop. Phys. 22 (2005) 387

JRH, Mod. Phys. Lett. A 22 (2007) 1533

Averaging over showers with an energy-independent mass composition of primary particles does not change this result as we have from the superposition model $X_{\max} \propto D_{10}^{\text{had}} \log(E_0/A)$. However, a change of the primary composition is directly reflected in the elongation rate through

$$D_{10} = D_{10}^{\text{had}} \left(1 - \frac{\mathrm{d}\langle \ln A \rangle}{\mathrm{d} \log E}\right) \tag{16.26}$$

In general, in the presence of rising cross sections and violation of Feynman scaling as observed at colliders, the inelasticity of interactions increases with energy. As a consequence, the elongation rate of hadronic showers is always smaller than that of electromagnetic showers. Hence, observing an elongation rate similar or larger than 85 g/cm^2 is a very strong indication of a change of the mass composition toward a lighter mix of primary particles.

16.6 Shower universality and cross section measurement

By the 1980s Hillas had already pointed out that electromagnetic showers exhibit universality features [527]. The prediction of cascade theory for the mean longitudinal profile of EM showers being only a function of shower age s can be extended to individual showers. By introducing the empirical definition of shower age

$$s = \frac{3}{1 + 2X_{\max}/X}, \tag{16.27}$$

each individual shower profile can be considered as function of this age parameter. As simulations show, the normalized shower profiles are reasonably well described by a single universal profile, independent of primary energy and even of the mass composition [528, 529]. The origin of this universality lies in the nature of the cascade process for large particle numbers and is related to particle multiplication and absorption reaching an equilibrium at shower maximum, washing out any initial fluctuations [530]. For high-energy showers ($E \gtrsim 10^{17}$ eV), essentially all relevant quantities of shower particles such as energy, angle and time distributions can be parametrized as functions of shower age and lateral distance scaled by the Molière unit [504, 531]. Such parametrizations are particularly useful for estimating the Cherenkov light contribution [532] to the shower signal measured with fluorescence telescopes. Very powerful shower reconstruction methods can be developed by employing universality features to obtain an effective multivariate analysis of all observables [533].

Astroparticle Physics 31 (2009) 243–254

Contents lists available at ScienceDirect

Astroparticle Physics

journal homepage: www.elsevier.com/locate/astropart

Universality of electron–positron distributions in extensive air showers

S. Lafebre [a,*], R. Engel [b], H. Falcke [a,c], J. Hörandel [a], T. Huege [b], J. Kuijpers [a], R. Ulrich [b]

3. Longitudinal description

There are several ways to describe the longitudinal evolution of an air shower.

Slant depth X measures the amount of matter an air shower has traversed in the atmosphere, in g/cm^2.

Relative evolution stage is defined here in terms of the depth relative to the slant depth $X_{\max}$, where the number of particles in the air shower reaches its maximum

$$t \equiv \frac{X - X_{\max}}{X_0}, \tag{1}$$

with $X_0 \simeq 36.7\,\mathrm{g/cm^2}$ being the radiation length of electrons in air. Because the shower maximum always lies at $t = 0$, describing multiple showers in terms of this quantity rather than X is expected to lead to a higher degree of universality.

Shower age is defined here so that $s = 0$ at the top of the atmosphere, $s = 1$ at the shower maximum, and $s = 3$ at infinite depth

$$s \equiv \frac{3X}{X + 2X_{\max}} = \frac{t + X_{\max}/X_0}{t/3 + X_{\max}/X_0}. \tag{2}$$

The concept of shower age arises naturally from cascade theory in purely electromagnetic showers [3,27].

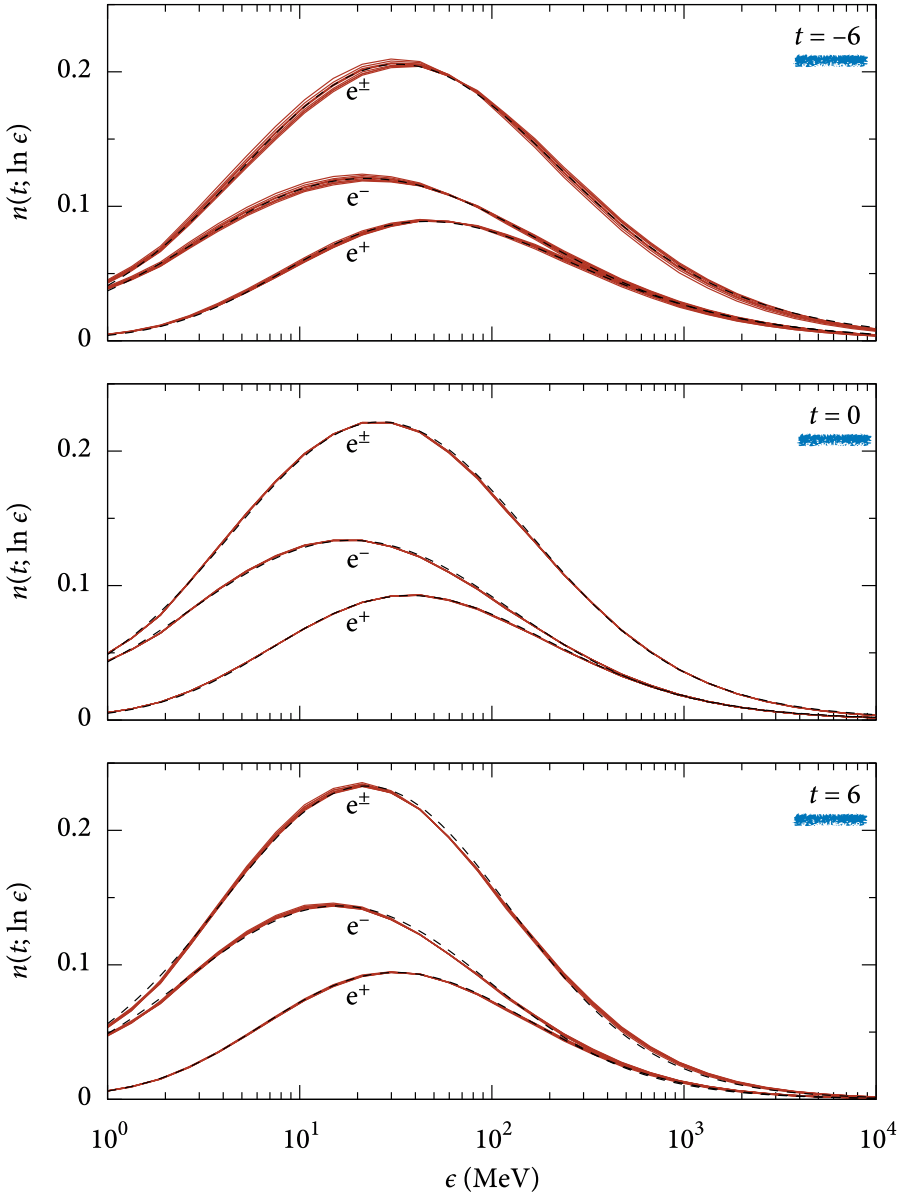

Fig. 2. Average energy distribution for different evolution stages $t = -6, 0, 6$ for electrons (marked e^-), positrons (e^+), and their sum ($e^\pm$). Background curves represent simulated distributions for different primaries (p, Fe, and γ) and energies ($10^{17}, 10^{18}$ and 10^{19} eV). The corresponding parameterized distributions from (6) are plotted on top (dashed).

4. Energy spectrum

From cascade theory, the energy spectrum of electrons and positrons as a function of shower age takes an analytical form as derived by Rossi and Greisen [3]; a thorough previous study of this parameterization was done by Nerling et al. [10]. Loosely translating this description in terms of t, we replace the equation by

$$n(t; \ln \epsilon) = \frac{A_0 \epsilon^{\gamma_1}}{(\epsilon + \epsilon_1)^{\gamma_1} (\epsilon + \epsilon_2)^{\gamma_2}}, \tag{6}$$

where ϵ is the energy of a given secondary particle in the shower, and $\epsilon_{1,2}$ depend on t. We have performed a fit to this function for electrons, positrons and their sum, indirectly providing a description of the negative charge excess of extensive air showers as a function of evolution stage and secondary energy. In these fits the exponent γ_1 was fixed at $\gamma_1 = 2$ for positrons and $\gamma_1 = 1$ for both electrons and the total number of particles. The parameters for all three cases are explained in Appendix A.1.

S. Lafebre et al. / Astroparticle Physics 31 (2009) 243–254

5. Angular spectrum

The angular distribution of particles is an important factor for observations with Cherenkov and radio telescopes. For successful radio detection an antenna needs to be placed close to the shower impact position, because geosynchrotron radiation is beamed in a very narrow cone in the direction of propagation [33]. As far as the particle distributions are concerned, the size of the patch that is illuminated on the ground then depends on the lateral distribution of the particles (cf. Section 7) and the angle with respect to the shower axis at which they propagate. Likewise, for Cherenkov observations the angle at which photons are emitted is a convolution of the density-dependent Cherenkov angle, which is of the order of $\sim 1^\circ$, and the angular distribution of the particles that emit them.

To compensate for the increase in solid angle with rising θ, the distribution of vertical momentum angles plotted here is defined in terms of Ω as

$$n(t;\ln\epsilon,\Omega) = \frac{n(t;\ln\epsilon,\theta)}{\sin\theta}. \quad (7)$$

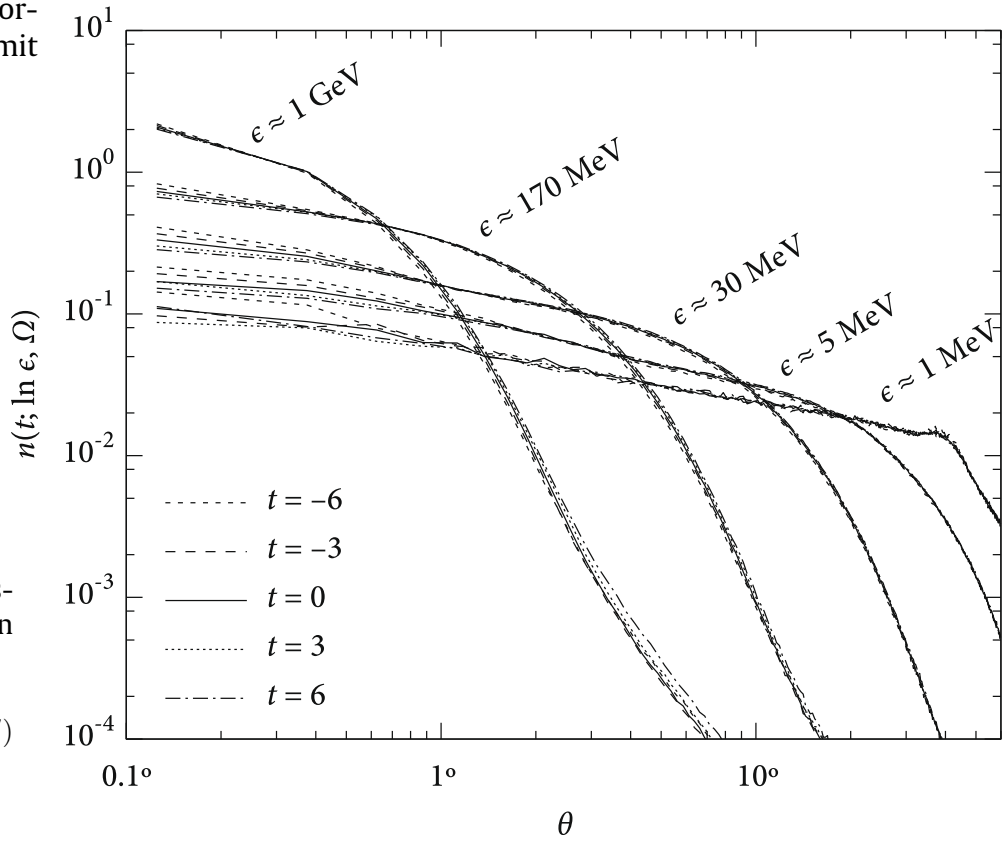

Fig. 4. Normalized average distributions $n(t;\ln\epsilon,\Omega)$ for different shower stages, averaged over 20 proton-initiated showers at 10^{18} eV.

The universality with respect to t allows us to parameterize this distribution as a function of two physical quantities only: momentum angle and energy. We propose the form

$$n(t;\ln\epsilon,\Omega) = C_0\left[\left(e^{b_1}\theta^{\alpha_1}\right)^{-1/\sigma} + \left(e^{b_2}\theta^{\alpha_2}\right)^{-1/\sigma}\right]^{-\sigma}, \tag{8}$$

to describe the distribution. Values for α_i and b_i, which envelop the dependence on ϵ, are chosen such that the first term describes the flatter portion of the angular distribution parallel to the shower axis and the second represents the steep drop. The value of σ determines the smoothness of the transition from the flat region to the steep region. Best fit values for σ, b_i, and α_i are given in Append

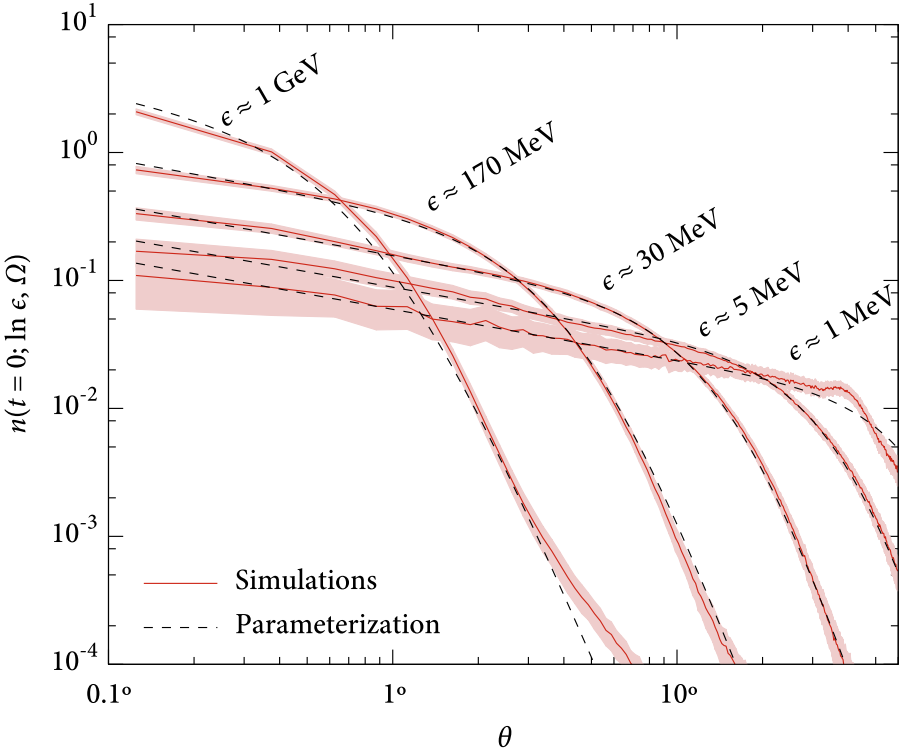

Fig. 5. Normalized average electron distributions $n(t=0;\ln\epsilon,\Omega)$ (solid) for 20 proton showers at 10^{18} eV with 3σ statistical error margins (filled area). For each energy, corresponding parameterizations according to (8) are also drawn (dashed).

7. Lateral distribution

The lateral spread of particles in an air shower is of direct relevance since it is the primary means of obtaining information about the shower in ground-based scintillator experiments measuring particle densities at different lateral distances. By integrating the measured distribution or using the particle density at a given distance, an estimate for the primary energy can be made. Exact knowledge of the lateral distribution shape is therefore crucial to accurately determine the shape of the cosmic-ray energy spectrum.

When looking at the lateral distribution of electron and positrons in terms of the lateral distance r from the shower axis, a very poor level of universality is encountered. This is mainly due to differences in atmospheric density at the individual values of $X_{\max}$. We can compensate for these differences by expressing the lateral distance in terms of the Moliére unit r_M, defining [35]

$$x \equiv \frac{r}{r_M} \simeq \frac{r\rho_A(h)}{9.6\,\mathrm{g/cm^2}}, \tag{11}$$

where $\rho_A(h)$ is the atmospheric density as a function of height h. For different values of ϵ, the normalized lateral particle distribution at $t = 0$ is shown in Fig. 9 as a function of distance for 20 individual proton showers. In this figure, all curves line up as the compensation for density is applied. Note that the physical density $N(t;r)$, expressed in particles per unit area, is proportional to $N(t;\ln x)/x^2$:

$$N(t;\ln x) = \frac{\partial N(t)}{\partial \ln x} = 2\pi x^2 r_M^2 \frac{\mathrm{N}(t)}{2\pi r\ dr}, \tag{12}$$

and decreases strictly with distance from the shower axis. As expected, particles with higher energies tend to remain closer to the shower axis. This agrees with the observation that the angle of their momentum to the shower axis is smaller.

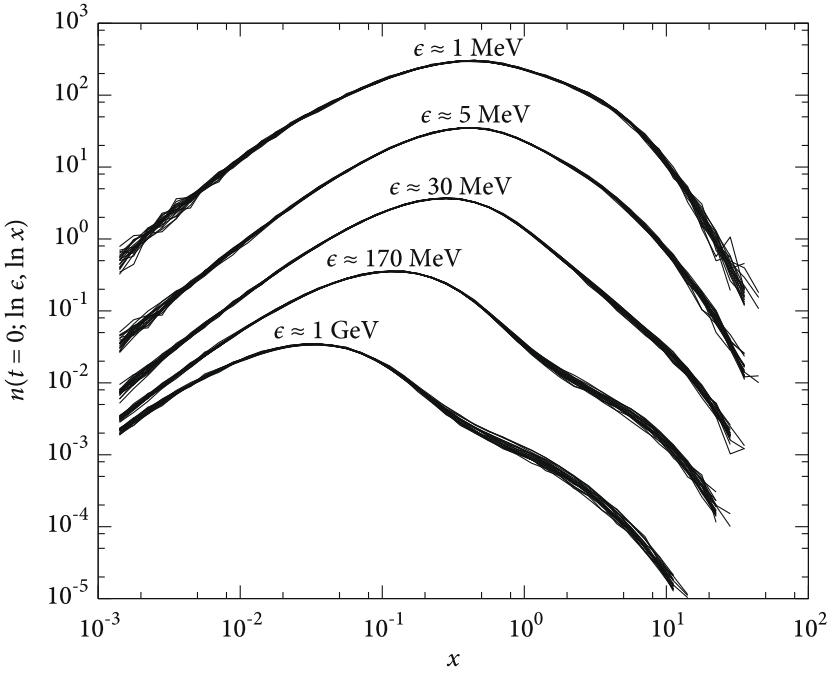

Fig. 9. Electron distributions $n(t = 0;\ln\epsilon,\ln x)$ for different electron energies as a function of distance to the shower axis for 20 individual showers initiated by 10^{18} eV protons. The curve set for 1 GeV is at the actual level; consecutive sets are shifted up by a factor of 10.

There is no statistically relevant dependence of the lateral distribution on zenith angle of incidence, nor does it change when electrons or positrons are considered separately, except at energies $\epsilon < 10\,\mathrm{MeV}$. There is, however, a significant effect with shower stage as shown in Fig. 10: older showers tend to be wider at the same secondary energy. Therefore, unlike in the case of angular distributions, in any parameterization of the lateral distribution a dependence on t must be incorporated. There is also a minor effect of the energy of the primary on the distribution, but this is only appreciable for secondary energies of $\epsilon > 1\,\mathrm{GeV}$.

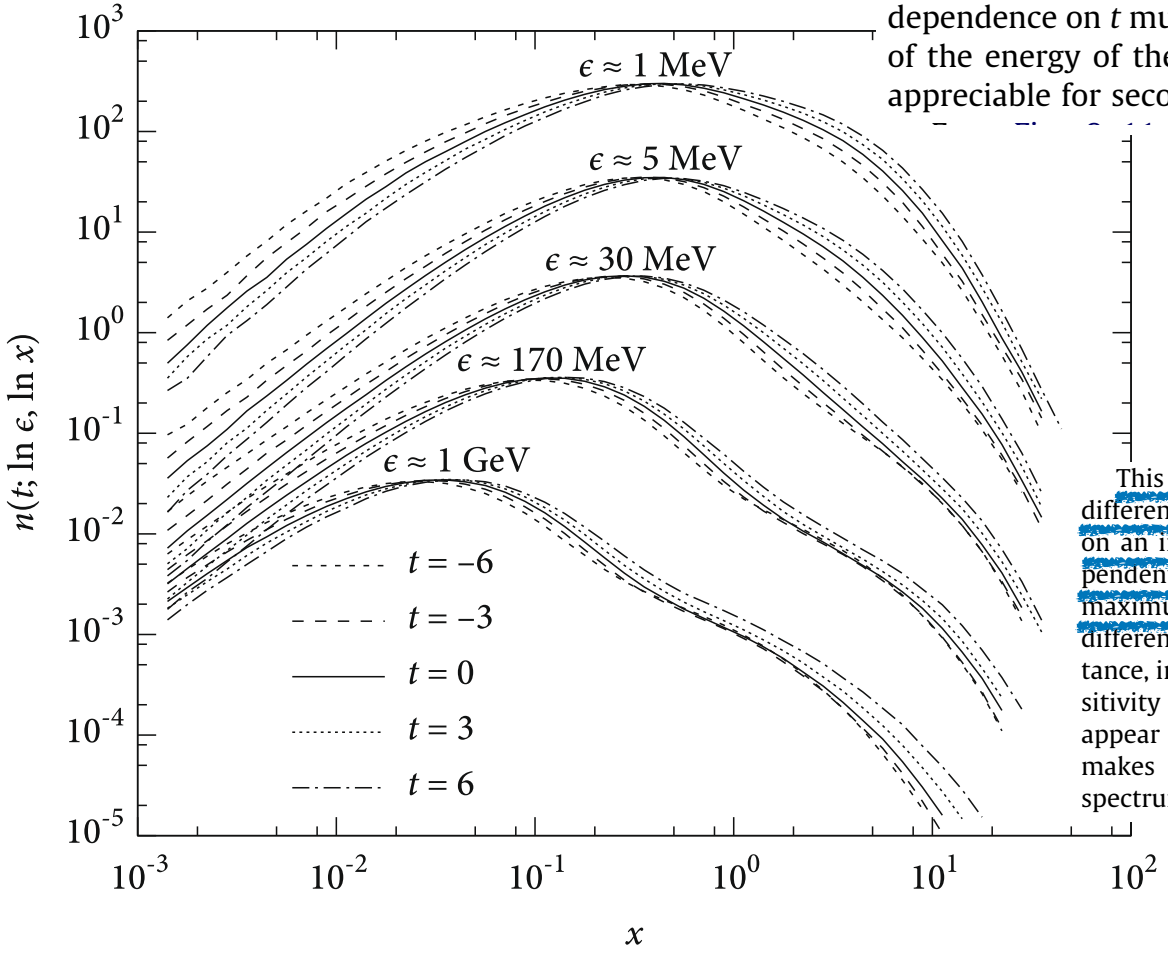

This observation raises the question whether one could use this difference in lateral distribution to differentiate between primaries on an individual shower basis by their lateral distribution, independently of measurements of primary energy or depth of shower maximum. This would be a difficult task. First of all, appreciable difference in density only occurs at high energies and at some distance, implying that the total electron density in the region of sensitivity would be very small. Additionally, the effect does not appear at the same distance for different electron energies. This makes the feature less pronounced when an integrated energy spectrum is measured.

Fig. 10. Average distributions $n(t; \ln\epsilon, \ln x)$ for different shower stages, averaged over 20 proton-initiated showers at $10^{18}\,\mathrm{eV}$, clearly showing dependence on t. Again, consecutive sets are shifted up by a factor of 10.

Traditionally, the integral lateral electron distribution is described by an approximation of the analytical calculation of the lateral distribution in electromagnetic cascades, the Nishimura–Kamata–Greisen (NKG) function [36,37]. The integral lateral distribution for our simulated set of showers $n(t;\ln x) \propto x^2 \rho_{\mathrm{nkg}}$ is reproduced well by a parameterization of this form, provided that we allow the parameters to be varied somewhat. Let us define

$$n(t;\ln x) = C_2 x^{\zeta_0} (x_1 + x)^{\zeta_1} \tag{13}$$

as parameterization. In the original definition, described in terms of shower age s, we have $\zeta_0 = s, \zeta_1 = s - 4.5$, and $x_1 = 1$. Our simulated lateral spectra closely follow the values $\zeta_0 = 0.0238t + 1.069, \zeta_1 = 0.0238t - 2.918$, and $x_1 = 0.430$ to an excellent level for $10^{-3} < x < 10$.

proton-air cross section

One application of shower universality is the measurement of the proton–air cross section with air showers. The depth of the first interaction point of a shower is exponentially distributed

$$\frac{\mathrm{d}P}{\mathrm{d}X_1} = \frac{1}{\lambda_{\mathrm{int}}} e^{-X_1/\lambda_{\mathrm{int}}}, \tag{16.28}$$

where λ_{int} is the interaction length, which is related to the particle production cross section σ_{prod} (see Eq. 4.82) by $\lambda_{\mathrm{int}} = \langle m_{\mathrm{air}} \rangle / \sigma_{\mathrm{prod}}$. It is, however, impossible to measure the early, low-multiplicity part of the shower development well enough to infer X_1 directly. Auxiliary quantities such as the depth of shower maximum, X_{max}, have to be used to derive information on the first interaction point. Indeed, the distribution of X_{max} is approximately exponential as expected from (16.28). The slope of this distribution, Λ, has to be converted to λ_{int} with detailed shower and detector simulations due to the importance of fluctuations. Simulations indicate that $\sim$ 50% of the size of the shower-to-shower fluctuations of X_{max} of proton showers are due to the fluctuations of the first interaction point, for which we have $\mathrm{RMS}(X_1) = \lambda_{\mathrm{int}}$.

In addition to the need for correcting for shower-to-shower fluctuations, cross section measurements are also subject to uncertainties arising from the unknown primary mass composition. Typically showers with very deep $X_{\max}$ are selected to suppress the contamination by heavier primaries.

A compilation of p-air cross section measurements is shown in Figure 16.4. The low-energy data are from experiments measuring the attenuation of the hadron flux in the atmosphere and the high-energy results are based on air shower measurements in combination with universality assumptions; see [535] for an overview of the different measurement methods, where also the references to the original work are given.

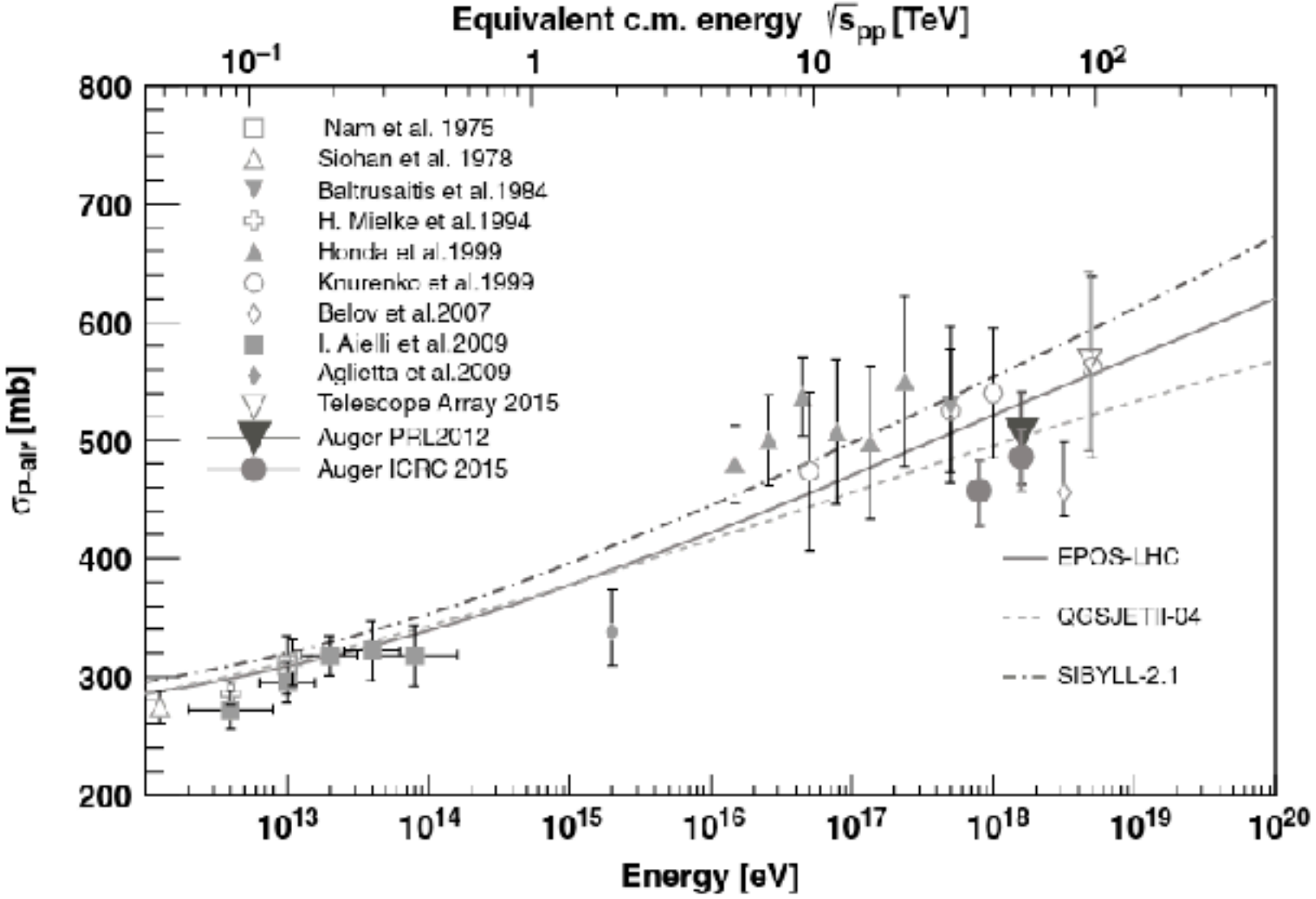

Figure 16.4 Proton–air cross section measured with cosmic ray experiments. The data are compared to predictions of hadronic interaction models. From Ref. [534], where also the references to the data and models are given.

Measurement of the Proton-Air Cross Section at $\sqrt{s} = 57$ TeV with the Pierre Auger Observatory

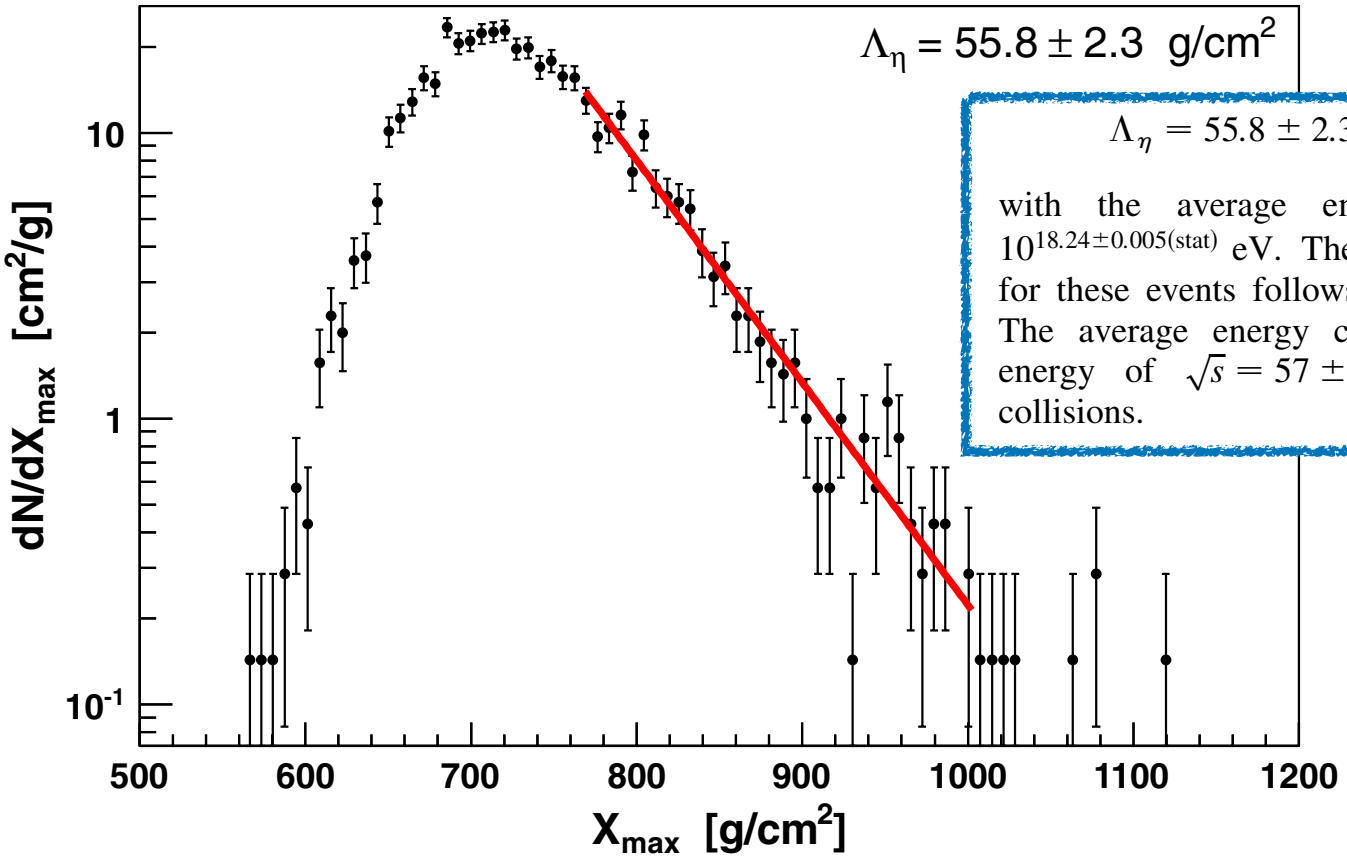

$$\Lambda_\eta = 55.8 \pm 2.3(\text{stat}) \pm 1.6(\text{syst})] \text{ g/cm}^2, \quad (1)$$

with the average energy of these events being $10^{18.24 \pm 0.005(\text{stat})}$ eV. The differential energy distribution for these events follows a power law with index -1.9. The average energy corresponds to a center-of-mass energy of $\sqrt{s} = 57 \pm 0.3(\text{stat})$ TeV in proton-proton collisions.

FIG. 1 (color online). Unbinned likelihood fit to obtain Λ_η (thick line). The $X_{\max}$ distribution is unbiased by the fiducial geometry selection applied in the range of the fit.

Determination of the cross section.—The determination of the proton-air cross section for particle production requires the use of air-shower simulations, which inherently introduces some dependence on model assumptions. We emulate the measurement of Λ_η with Monte Carlo simulations to derive predictions of the slope, $\Lambda_\eta^{\mathrm{MC}}$. It is known from previous work that the values of $\Lambda_\eta^{\mathrm{MC}}$ are directly linked to the hadronic cross sections used in the simulations [2]. Accordingly we can explore the effect

PHYSICAL REVIEW D VOLUME 26, NUMBER 1 1 JULY 1982

Ultrahigh-energy cross section from study of longitudinal development of air showers

R. W. Ellsworth
Department of Physics, George Mason University, Fairfax, Virginia 22030

T. K. Gaisser and Todor Stanev*
Bartol Research Foundation of The Franklin Institute, University of Delaware, Newark, Delaware 19711

G. B. Yodh
Department of Physics, University of Maryland, College Park, Maryland 20742
(Received 1 March 1982)

We present calculations of the type that will be necessary for interpretation of large cosmic-ray experiments that measure longitudinal profiles of individual showers. A primary goal of such experiments is to determine both cross section and composition around 10^{18} eV.

Even without the problem of heavy primaries, measurement of x_m or $x_{1/4}$ alone cannot determine an arbitrarily large proton cross section because of intrinsic fluctuations in shower development. The results of our calculations bear this out, as shown in Fig. 2. Here we show Λ_m for proton showers only, as a function of $\sigma_{p\text{-air}}$ at 3×10^{17} eV. For the atmosphere,

$$\lambda_{p\text{-air}}\ (\mathrm{g/cm^2}) = \frac{2.4 \times 10^4}{\sigma_{p\text{-air}}\ (\mathrm{mb})} \ .$$

We emphasize that Fig. 2 cannot at present be used for an accurate determination of $\sigma_{p\text{-air}}$ from Λ_m because of the dependence on composition mentioned above. In addition, possible effects of uncertainties in the interaction model and of instrumental fluctuations need to be understood.

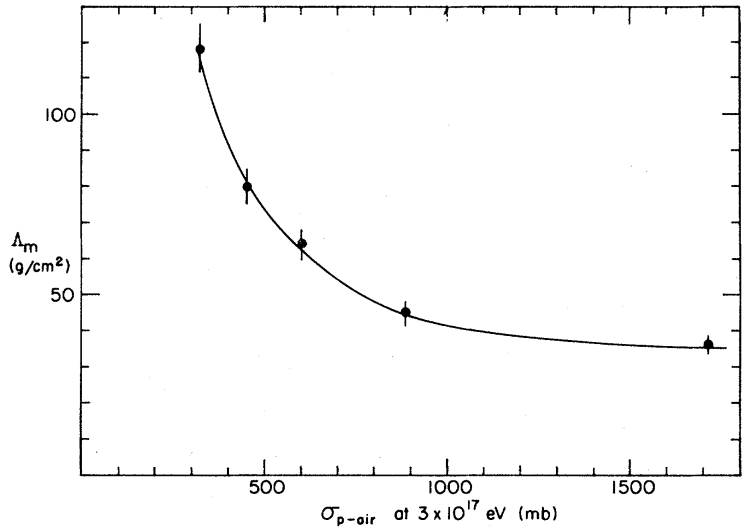

FIG. 2. Λ_m vs $\sigma_{p\text{-air}}$ for proton showers chosen from a power-law energy spectrum (differential index = 2) with $E_0 > 3 \times 10^{17}$ eV. Error bars show statistical uncertainty from the simulation result. Since the figure shows proton showers only, it cannot be used for an accurate determination of σ. See text.

Measurement of the Proton-Air Cross Section at $\sqrt{s} = 57$ TeV with the Pierre Auger Observatory

$$\sigma^{\text{prod}}_{p\text{-air}} = [505 \pm 22(\text{stat})^{+28}_{-36}(\text{syst})]\ \text{mb}$$

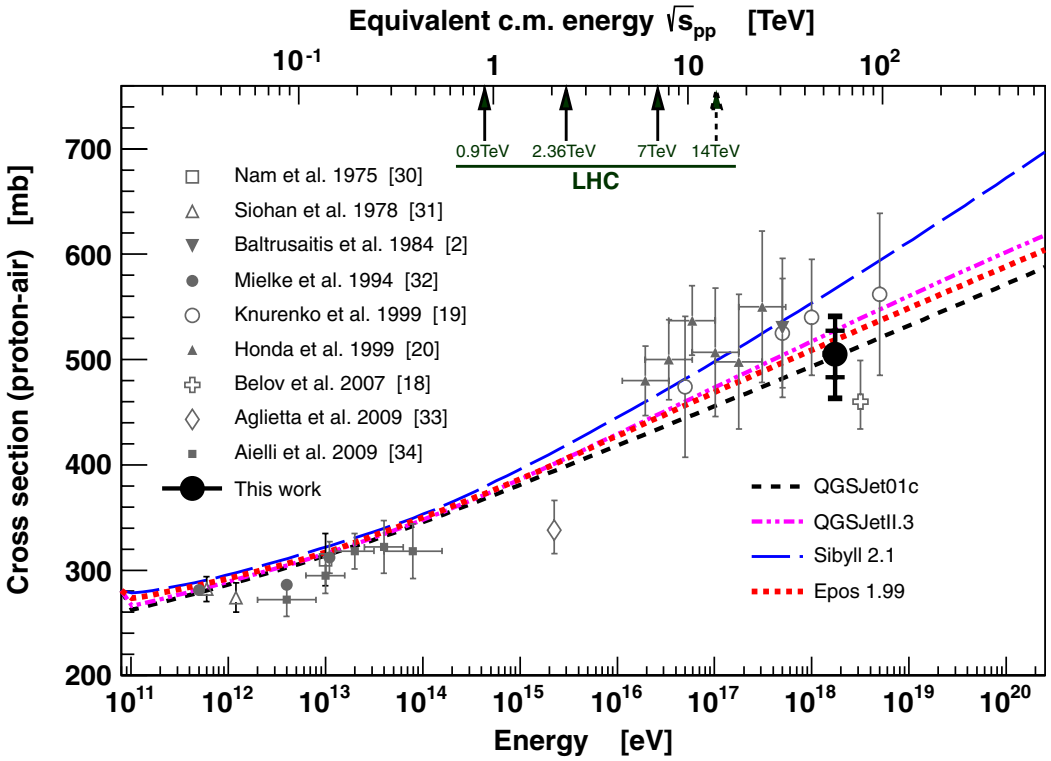

FIG. 2 (color online). Resulting $\sigma^{\text{prod}}_{p\text{-air}}$ compared to other measurements (see [18–20,30–34]) and model predictions. The inner error bars are statistical, while the outer include systematic uncertainties for a helium fraction of 25% and 10 mb for the systematic uncertainty attributed to the fraction of photons.

TABLE I. Summary of the systematic uncertainties.

Description	Impact on $\sigma^{\text{prod}}_{p\text{-air}}$
Λ_η systematics	± 15 mb
Hadronic interaction models	$-8 + 19$ mb
Energy scale	± 7 mb
Conversion of Λ_η to $\sigma^{\text{prod}}_{p\text{-air}}$	± 7 mb
Photons, $<0.5\%$	$< + 10$ mb
Helium, 10%	-12 mb
Helium, 25%	-30 mb
Helium, 50%	-80 mb
Total (25% helium)	-36 mb, $+28$ mb

Comparison with accelerator data.—For the purpose of making comparisons with accelerator data we calculate the inelastic and total proton-proton cross sections using the Glauber model. We use standard Glauber formalism [21],

This Glauber calculation is model-dependent since neither the parameters nor the physical processes involved are known accurately at cosmic-ray energies. In particular, this applies to the elastic slope parameter, $B_{\rm el}$ (defined by $d\sigma_{\rm el}/dt \propto \exp(-|t|B_{\rm el})$ for very small t), the correlation of $B_{\rm el}$ to the cross section, and the cross section for diffractive dissociation. For the example of $\sigma_{pp}^{\rm inel}$, the correlation of $B_{\rm el}$ with the cross section is shown in Fig. 3 for $\lambda = 0.5$. We have used the same four hadronic interaction models to determine the uncertainty band of the $B_{\rm el}$-$\sigma_{pp}^{\rm inel}$ correlation. Recent cross-section models such as [23] fall

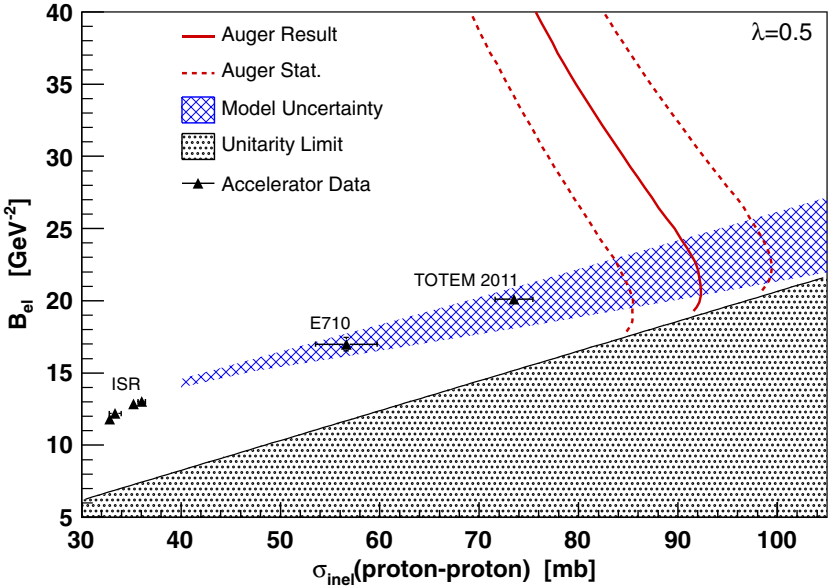

FIG. 3 (color online). Correlation of elastic slope parameter, $B_{\rm el}$, and the inelastic proton-proton cross section in the Glauber framework. The solid line indicates the parameter combinations yielding the observed proton-air production cross section, and the dotted lines are the statistical uncertainties. The hatched area corresponds to the predictions by SIBYLL, QGSJET, QGSJETII, and EPOS. See also Ref. [5].

Measurement of the Proton-Air Cross Section at $\sqrt{s} = 57$ TeV with the Pierre Auger Observatory

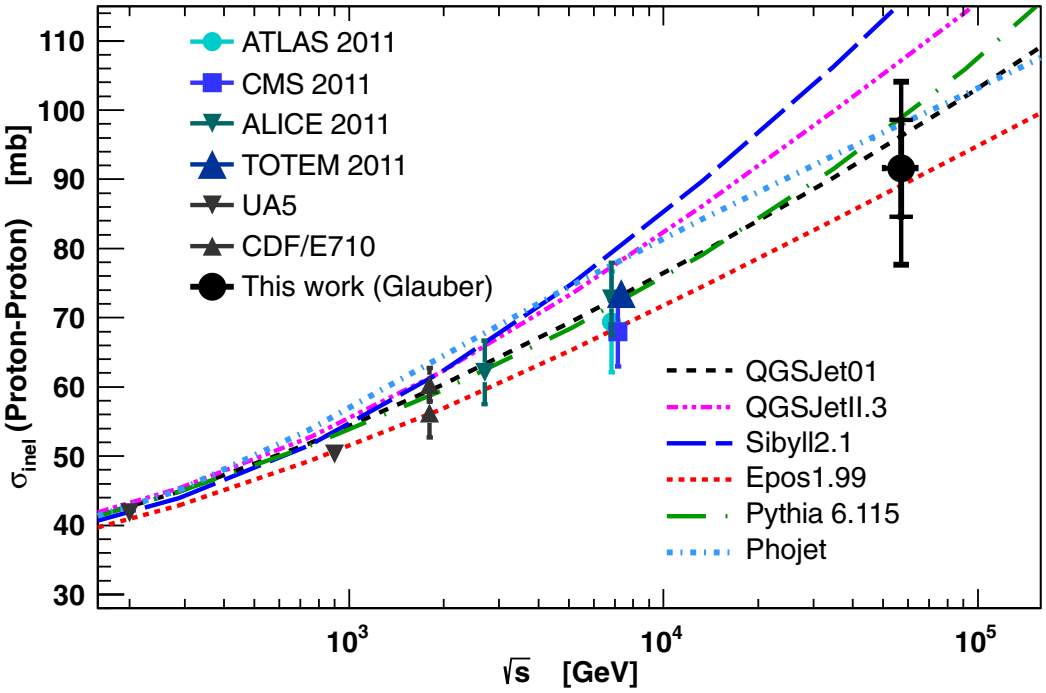

FIG. 4 (color online). Comparison of derived $\sigma_{pp}^{\text{inel}}$ to model predictions and accelerator data [29]. Here we also show the cross sections of two typical high-energy models, PYTHIA6 [35] and PHOJET [36]. The inner error bars are statistical, while the outer include systematic uncertainties.

We find that in the Glauber framework the *inelastic* cross section is less dependent on model assumptions than the *total* cross section. The result for the inelastic proton-proton cross section is

$$\sigma_{pp}^{\text{inel}} = [92 \pm 7(\text{stat})^{+9}_{-11}(\text{syst}) \pm 7(\text{Glauber})]\ \text{mb},$$

and the total proton-proton cross section is

$$\sigma_{pp}^{\text{tot}} = [133 \pm 13(\text{stat})^{+17}_{-20}(\text{syst}) \pm 16(\text{Glauber})]\ \text{mb}.$$

The systematic uncertainties for the inelastic and total cross sections include contributions from the elastic slope parameter, from λ, from the description of the nuclear density profile, and from cross-checking these effects using QGSJETII [9,24]. For the inelastic case, these three independent contributions are 1, 3, 5, and 4 mb, respectively. For the total cross section, they are 13, 6, 5, and 4 mb. We emphasize that the total theoretical uncertainty of converting the proton-air to a proton-proton cross section may be larger than estimated here within the Glauber model.